ACS Catalysis

Research Article

Cite This: ACS Catal. 2018, 8, 4408–4419

pubs.acs.org/acscatalysis

Climbing the Volcano of Electrocatalytic Activity while Avoiding Catalyst Corrosion: Ni_3P, a Hydrogen Evolution Electrocatalyst Stable in Both Acid and Alkali

Anders B. Laursen,[†] Robert B. Wexler,[‡] Marianna J. Whitaker,[†] Edward J. Izett,[†] Karin U. D. Calvinho,[†] Shinjae Hwang,[†] Ross Rucker,[§] Hao Wang,[†] Jing Li,[†] Eric Garfunkel,[†] Martha Greenblatt,*[,†] Andrew M. Rappe,*[,‡] and G. Charles Dismukes*[,†,∥]

[†]Department of Chemistry and Chemical Biology, Rutgers, The State University of New Jersey, 610 Taylor Road, Piscataway New Jersey 08854, United States

[‡]Department of Chemistry, University of Pennsylvania, 231 South 34th Street, Philadelphia, Pennsylvania 19104-6323, United States

[§]Department of Materials Science and Engineering, Rutgers, The State University of New Jersey, 607 Taylor Road, Piscataway New Jersey 088544, United States

[∥]Waksman Institute of Microbiology, Rutgers, The State University of New Jersey,190 Frelinghuysen Road, Piscataway, New Jersey 08854, United States

Supporting Information

ABSTRACT: We report microcrystalline Ni_3P as a noble-metal-free electrocatalyst for the H_2 evolution reaction (HER) with high activity just below those of Ni_5P_4 and Pt, the two most efficient HER catalysts known. Ni_3P has previously been dismissed for the HER, owing to its anticipated corrosion and its low activity when formed as an impurity in amorphous alloys. We observe higher activity of single-phase Ni_3P crystallites than for other nickel phosphides (except Ni_5P_4) in acid, high corrosion tolerance in acid, and zero corrosion in alkali. We compare its electrocatalytic performance, corrosion stability, and intrinsic turnover rate to those of different transition-metal phosphides. Electrochemical studies reveal that poisoning of surface Ni sites does not block the HER, indicating P as the active site. Using density functional theory (DFT), we analyze the thermodynamic stability of Ni_3P and compare it to experiments. DFT calculations predict that surface reconstruction of Ni_3P (001) strongly favors P enrichment of the Ni_4P_4 termination and that the H adsorption energy depends strongly on the surface reconstruction, thus revealing a potential synthetic lever for tuning HER catalytic activity. A particular P-enriched reconstructed surface on $Ni_3P(001)$ is predicted to be the most stable surface termination at intermediate P content, as well as providing the most active surface site at low overpotentials. The P adatoms present on this reconstructed surface are more active for HER at low overpotentials in comparison to any of the sites investigated on other terminations of $Ni_3P(001)$, as they possess nearly thermoneutral H adsorption. To our knowledge this is the first time reconstructed surfaces of transition-metal phosphides have been identified as having the most active surface site, with such good agreement with the experimentally observed catalytic current onset and Tafel slope. The active site geometry achieved through reconstruction identified in this work shows great similarity to that reported for $Ni_2P(0001)$ and $Ni_5P_4(0001)$ facets, serving as a general design principle for the future development of even more active transition-metal phosphide catalysts and further climbing the volcano plot.

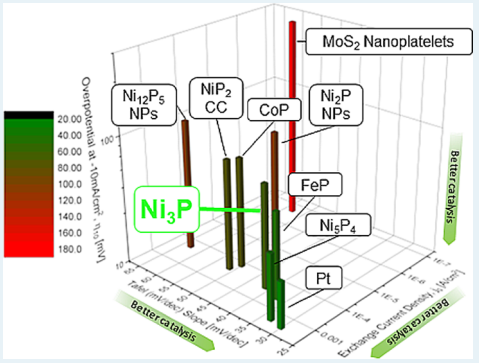

KEYWORDS: *water splitting, electrocatalysis, hydrogen evolution, HER, renewable energy, energy storage*

INTRODUCTION

Chief among the technical limitations preventing the development of a sustainable industry sector is the design of low-cost, nontoxic, renewable materials and the emergence of processes amenable to energy-intensive chemical conversions. These materials include catalysts for solar energy conversion, $CO_2(g)$ reduction, and $NH_3(g)$ synthesis. Renewable $H_2(g)$ production via water electrolysis is essential to all these technologies, yet it remains unrealized on an industrial scale, owing to the high cost of noble-metal catalysts and poor efficiencies in noncorrosive electrolytes.

The hydrogen evolution reaction (HER) proceeds readily on Pt in both acidic ($2H^+ + 2e^- \leftrightarrow H_2(g)$) and basic ($2H_2O + 2e^- \leftrightarrow 2OH^- + H_2(g)$) aqueous media. Pt requires a very low overpotential (η) of ~20 mV in acid (pH 0) and 163 mV in

Received: December 27, 2017
Revised: March 26, 2018
Published: April 3, 2018

DOI: 10.1021/acscatal.7b04466
ACS Catal. 2018, 8, 4408–4419

alkali (pH 14) for yielding a current density of −10 mA/cm$^2_{geo}$ (η_{10}).[1] This current density corresponds to 10% solar to hydrogen efficiency, which is one of the U.S. Department of Energy's benchmarks for commercialization.[2] Although Pt exhibits good electrical conductivity and high corrosion tolerance in strongly acidic and alkaline electrolytes, it is too scarce for global application at any pH. Ru nanoparticles supported on C−N materials[3] have shown great promise as state of the art HER catalysts in both alkali and acid. While the low abundance of ruthenium may limit its application on a global scale,[4] understanding the HER mechanism on this material could lead to the discovery of chemically intuitive metrics that govern electrocatalysis and can be tuned to optimize catalyst efficiency.

To address the need for inexpensive, noble-metal-free HER catalysts, several transition-metal nitride,[5] sulfide,[6−12] and phosphide[1,13−15,15,16] compounds have been identified, as well as transition-metal-doped N/S/P-functionalized carbon hybrid materials.[17] The reported performance (overpotentials) of these catalysts is summarized in Table S1. Notable examples include various morphologies of MoS_2 (η_{10} = 150−202 mV[7,18,19] at pH 0), CoP nanoparticles (75 mV at pH 0),[13] and nanocrystalline Ni_5P_4 microparticles (nc-MPs, 33 mV at pH −0.04).[16] nc-MPs are nanocrystals that agglomerate into microparticles while retaining some of their nanoroughness. The activity of Ni_5P_4 nc-MPs is comparable to that of the benchmark HER catalyst, polycrystalline Pt foil, which requires η_{10} = 27 mV under identical conditions.[16] Due to its high electrical conductivity,[16] Ni_5P_4 can even be used without a conductive support, which simplifies electrode design and allows for very high loadings and corresponding high currents per unit electrolyzer area. Of the six known thermodynamically stable (<800 °C) crystalline nickel phosphide compounds (Ni_3P,[20] Ni_5P_2, $Ni_{12}P_5$,[21] Ni_2P,[1,22,23] Ni_5P_4,[16,24] and NiP_2[25]), most of them exhibit good HER catalytic activity (η_{10} < 150 mV) in acid (pH 0), with Ni_5P_4 being the best.[16,24]

Another requirement for a suitable catalyst is stability against corrosion under catalytic conditions. Pure Ni catalysts are used in commercial alkaline electrolyzers but show low activity and readily dissolve in acid (and very strong alkali), even under electrolysis conditions.[26] Ni corrosion is suppressed by combining it with P to form amorphous alloys (<30 atom % P) and stoichiometric Ni_xP_y crystalline compounds (≥25 atom % P). It was previously proposed that the corrosion tolerance of Ni_xP_y compounds improves with increasing P content,[27] since NiP_2 displays better stability toward oxidation than Ni_2P (this trend holds true for Mn, Fe, and Co phosphides as well).[27] We recently found that Ni_5P_4 has superior corrosion tolerance in both strong acid and alkali in comparison to Ni_2P, as the latter readily leaches Ni (50 atom % Ni over 16 h[16]). As such, Ni_5P_4 is one of the most active, corrosion-tolerant HER catalysts reported to date.[16] These observations suggest that Ni_xP_y with lower P content would be not only less HER active but also more susceptible to corrosion. To the best of our knowledge, however, there have not been any systematic studies of the corrosion tolerance of nickel phosphide compounds.

The HER activity trend for nickel phosphides is $Ni_{12}P_5$ < Ni_2P < Ni_5P_4.[28] This trend shows that HER activity is positively correlated with P content for crystalline nickel phosphides. For amorphous solid solutions of Ni and P, the optimal HER activity is attained at 12.5 atom % P.[29,30] The difference between the optimal P content for crystalline and amorphous nickel phosphides indicates a structural influence on HER activity.

A recent study[20] showed that multifaceted, nanoporous Ni_3P particles (synthesized using a low-temperature method that likely traps nonequilibrium surface phases) offer fairly good HER activity in acid (η_{10} = 85 mV and Tafel slope 50 mV/dec). The performance of this catalyst is significantly lower in comparison to ours (η_{10} = 66 mV and Tafel slope 41 mV/dec), and moreover the change in Tafel slope indicates a difference in the rate-determining kinetics of the former in comparison to the large domain crystalline particles (high-temperature synthesis) investigated in this work.

In this work, we investigate the HER activity and electrochemical stability of Ni_3P, which has the lowest P content of the thermodynamically stable nickel phosphide crystal phases, and it is therefore an important member of the nickel phosphide catalyst family. Ni_3P is especially appealing due to its excellent HER activity (even if it is lower than that of Ni_5P_4), its facile synthesis using low temperatures which allows for the synthesis of small nanocluster, and its ability to produce thin-film coatings—unlike the P-rich nickel phosphides.[29,31] We apply density functional theory calculations (DFT) to identify catalytically active sites on the (001) surface of Ni_3P and its reconstructions. We note that in the mineralogy literature it is well-known that the Ni_3P(001) facet is the preferred facet of cleaving for the isostructural schreibersite mineral; this mineral may also cleave imperfectly (forming less stable surfaces) along the (010) and (110) facets.[32] We thus investigate the surface energy of the bulk termination of these alternative facets in the composition region of Ni_3P stability (see the Supporting Information). This analysis supports the experimental observation that the (001) facet is the dominant facet over the entire compositional region of stability for phase-pure Ni_3P. The high-temperature synthesis ensures that the thermodynamically preferred (001) facet should be the major exposed facet according to the Wolf theory. We show that crystalline, phase-pure Ni_3P exhibits excellent HER activity (slightly lower than that of Ni_5P_4 and Pt, the best known HER catalysts) and high corrosion tolerance in both acid and alkali despite its low P content. We find that the stability of Ni_3P against electrochemical corrosion can be explained by its enthalpy of formation; Ni_3P has greater thermodynamic stability per atom than Ni and HER-active Ni alloys, such as NiMo. Our DFT calculations support this interpretation and indicate that a particular surface reconstruction of Ni_3P is thermodynamically favored. This surface reconstruction enables shallower binding energies of adsorbed H atoms, thereby creating more efficient, faster catalysis.

EXPERIMENTAL SECTION

Solid-State Catalyst Synthesis. Ni(s) and P(s) were reacted in evacuated quartz tubes at 700 °C for 24 h by a conventional solid-state reaction (see the Supporting Information for details).

Electrode Fabrication. A 100 mg portion of the catalyst and 250 μL of 5% Nafion (neutralized with NaOH) were combined, pressed into a pellet, and mounted as an electrode. Contacts and pellet sides were masked off with epoxy, leaving only the active surface area accessible to electrolyte (see the Supporting Information for details).

Electrochemical Measurements. All solutions were prepared using Millipore water. A piranha-cleaned three-electrode cell, with a Selemion membrane or porous glass frit

DOI: 10.1021/acscatal.7b04466
ACS Catal. 2018, 8, 4408−4419

separating working and counter compartments, was used for all of the electrochemical measurements. A B-doped diamond electrode was used as the counter electrode—avoiding any Pt source. Reference electrode potentials were calibrated to the RHE scale daily; the absence of any detectable Pt dissolution during calibration of the reference electrode was verified by ICP-OES ($LOD_{\alpha=0.05}$ = 0.2 ppm, see the Supporting Information for details). Solution resistances on the order of <10 Ω were corrected manually.

Computational Methodology. DFT[32,33] calculations were carried out using the Quantum Espresso code.[34] Optimized norm-conserving,[35] designed[36] pseudopotentials were constructed using the OPIUM code[37] for both Ni and P to soften their valence electron wave functions and ionic potentials. Wave functions were expanded in a plane-wave basis with a cutoff energy of 50 Ry. The exchange correlation energy was calculated using Perdew, Burke, and Ernzerhof's form of the generalized gradient approximation (GGA).[38] van der Waals interactions were treated using Grimme's semiempirical DFT-D2 method.[39,40]

RESULTS

Synthesis and Characterization. We synthesized Ni_3P and Ni_5P_4 using a solid-state procedure, modified from ref 41, at high temperature, so as to ensure uniform high crystallinity (for details see the Supporting Information). This solid-state synthesis method produces quantitative yields (in Ni) of single-phase Ni_5P_4. The as-synthesized Ni_3P MPs contain a small Ni(*s*) impurity, which was removed by washing the product in 15 wt % HCl for several hours with stirring under an inert N_2 atmosphere. A single-phase Ni_3P product was recovered by filtration. The complete removal of the Ni(*s*) impurity and absence of any other impurities before catalysis was verified by SEM-EDS measurements on 13 selected spots, which gave an average formal composition of $Ni_{3.1\pm0.3}P$ (see the Supporting Information). We confirmed the phase purity of Ni_3P (ICSD reference pattern: PDF 074-1384) and Ni_5P_4 (PDF 018-0883; Supporting Information) using Rietveld refinement of the powder X-ray diffraction (PXRD) (see Figure 1A and the Supporting Information). We find that Ni_3P MPs (Figure 1B) and Ni_5P_4 MPs (Supporting Information) have similar particle sizes in the range of 2−11 μm and therefore nearly identical N_2 adsorption BET surface areas of 0.11 and 0.10 m^2/g, respectively. As expected, our solid-state synthesis results in lower surface areas relative to those reported in other studies: e.g., our solvothermal route[16] to Ni_5P_4 nc-MPs (5.19 m^2/g).

Next, we describe the fabrication and evaluation of electrodes. We prepared electrodes by pressing a mixture of powdered catalyst and Nafion into pellets. We then mounted these pellets as the working electrode (see the Supporting Information). The addition of Nafion serves two purposes: (1) it increases proton conduction to the catalyst surface in acidic electrolytes and (2) it binds particles for enhanced mechanical stability during $H_2(g)$ evolution. In alkaline electrolytes, Nafion only serves to bind the catalyst because its sulfonic acid group, i.e. the proton source, is converted to sodium sulfonate (Na-Nafion). To utilize this fabrication method, electrodes must exhibit excellent electrical conductivity. Using a four-point probe measurement, the electrical resistivity of a pressed pellet of the pure Ni_3P powder is 4×10^{-6} Ω m (7×10^{-6} Ω m for Ni_5P_4). On the basis of this value, the estimated resistance across a representative pellet (480 μm thick and a geometric surface area of 0.03 cm^2) is 6×10^{-6} Ω (1×10^{-5} Ω for Ni_5P_4).

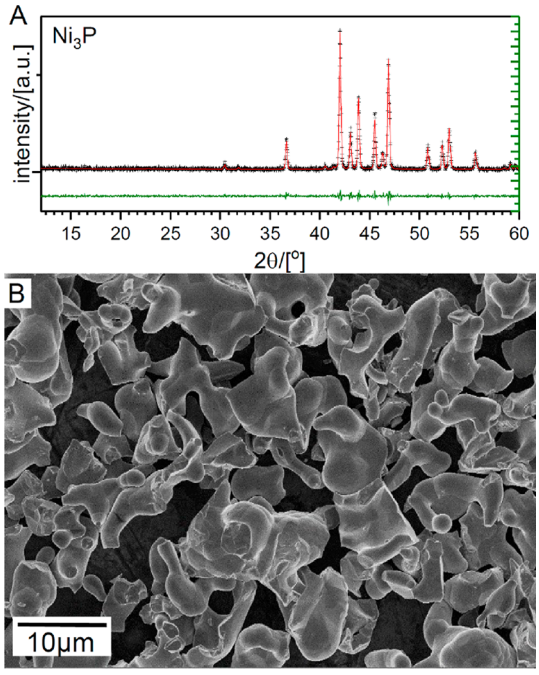

Figure 1. (A) PXRD pattern (in black) and Rietveld refinement fit for randomly oriented powder of Ni_3P (in red). The goodness of fit (χ^2) is χ^2 = 1.15 ± 0.03. (B) Scanning electron micrograph of Ni_3P microparticles synthesized using our solid-state method. Corresponding PXRD and SEM data for Ni_5P_4 microparticles reveal similarly excellent goodness of fit (χ^2 = 1.65 ± 0.11) and similar particle size distribution (see the Supporting Information).

The solution resistance (*iR* drop), which includes the resistance across the pellet, is relatively low (10−12 Ω), thus showing that the resistance across the pellet contributes only negligibly to the total resistance.

We evaluated electrochemical performance, catalyst durability, and reaction kinetics, using chronopotentiometry (CP) and cyclic voltammetry (CV), respectively. We corrected the measured potential for the uncompensated solution resistance and referenced it to the reversible hydrogen electrode (RHE) so that it does not change with pH. Figure 2A shows a CP analysis of different catalysts in 0.5 M H_2SO_4 (pH 0) and 1 M NaOH (pH 14) over 16 h. The potential of Pt in acid (−0.020 V vs RHE) is shown for comparison. Due to the rapid poisoning of Pt, even in high-purity solvents,[29] we report the potential required for a −10 mA/cm^2_{geo} kinetic current (determined from the CV measurement in Figure 2B). This potential value is a lower limit where the effect of contaminants and diffusion limits are excluded. This is compared to the static conditions of CP analysis of the nickel phosphides, where these effects are included. In acidic solution (0.5 M H_2SO_4), Ni_3P and Ni_5P_4 MPs require −0.066 and −0.043 V vs RHE, respectively, to drive a steady −10 mA/cm^2_{geo} current density of H_2 evolution for 16 h. In alkaline solution (1 M NaOH), Ni_3P and Ni_5P_4 require −0.291 and −0.193 V vs RHE, respectively. Both Ni_3P and Ni_5P_4 show an initial activation period (t < 2 h) in acid, after which there is no change in catalytic activity throughout the CP analysis. Under alkali conditions there is an initial decrease of activity at t < 2 h. These break-in periods are due to the reduction of the surface phosphorus oxide, in agreement with previous reports,[16] after which no further change in activity is observed, indicating catalyst stability.

DOI: 10.1021/acscatal.7b04466
ACS Catal. 2018, 8, 4408−4419

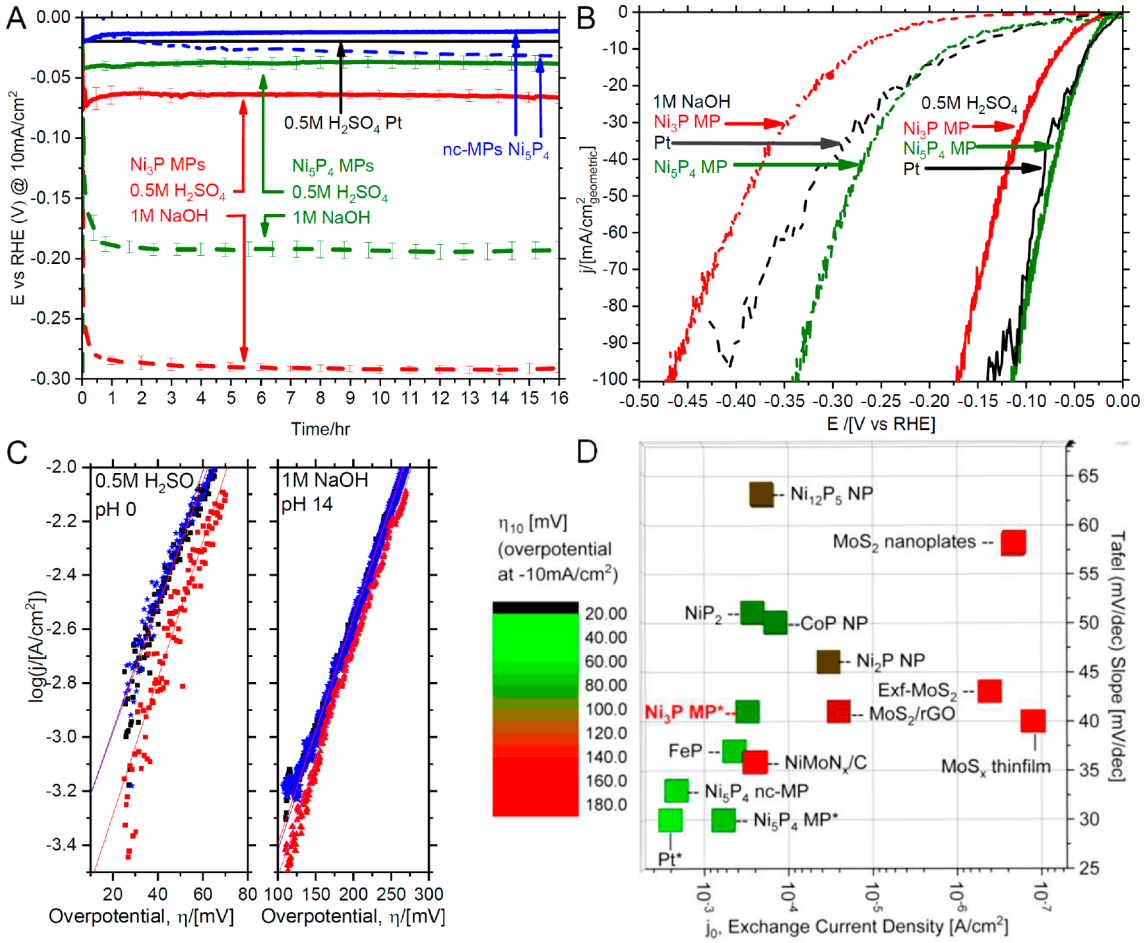

Figure 2. (A) CP analysis of Pt (in black), Ni_3P MPs (in red), and Ni_5P_4 MPs (in green) in 0.5 M H_2SO_4 (solid line) and 1 M NaOH (dashed line). For comparison, we also show Ni_5P_4 nc-MPs without Nafion (in blue), which is prepared using our solvothermal synthesis.[16] (B) CV measurements of Ni_3P (in red) and Ni_5P_4 (in green) in 0.5 M H_2SO_4 (solid line) and 1 M NaOH (dashed line) at a scan rate of 1 mV/s and under 1 atm of $H_2(g)$. (C) Tafel plots of Ni_3P in 0.5 M H_2SO_4 (left) and 1 M NaOH (right). Tafel analysis is performed on three individual electrodes and averaged to reduce capacitive current contributions. CV measurements of Pt foil are recorded as linear sweeps at fast scan rates (100 mV/s) to avoid mass transport limitations. (D) Comparison of three electrocatalyst performance metrics (Tafel slope, exchange current density, and the HER overpotential at -10 mA/cm^2_{geo}) for Ni_3P MPs and other state of the art HER electrocatalysts at pH 0 (see Figure S2 for pH 14). Asterisks indicate measurements presented in this work; all other measurements are based on literature reports.

Figure 2B shows a kinetic analysis (CV) of Ni_3P MPs, Ni_5P_4 MPs, and Pt in acid (solid lines) and base (dashed lines). We note that the noise in the traces of the Pt foil (and, to a lesser extent, the Ni_3P and Ni_5P_4 MPs) is due to H_2 bubble formation and release. This is not a weakness in the experimental design but rather an additional validation of HER catalytic activity. In acidic solution, the CV curve of Ni_5P_4 MPs (2−11 μm, solid state synthesis) overlaps that of Pt; the same result is observed for Ni_5P_4 nc-MPs (0.3−1.8 μm, solvothermal synthesis). Ni_3P MPs show performance comparable to that of Ni_5P_4 in acid but lower activity in alkaline solution, in agreement with the CP experiment above.

We measured the Faradaic yield of $H_2(g)$ using gas chromatography (GC) and found it to be 99 ± 16% in 0.5 M H_2SO_4 and 106 ± 12% in 1 M NaOH. This shows that $H_2(g)$ is the only gaseous reaction product. Due to the initial reduction of a surface oxide/phosphate (in agreement with previous observations[16]), the Faradaic yield was determined after ∼15 min of preconditioning. The quantitative yield of $H_2(g)$, within the uncertainty, indicates that Ni_3P does not leach Ni or P. To conclusively determine if the catalyst is stable against leaching and electrolytic corrosion under catalytic conditions, we measured the amount of dissolved Ni at different times using ICP-OES (see Table 1). In alkaline solution, we did not detect Ni, above the limit of detection ($LOD_{\alpha=0.05}$ = 0.16 ppm of Ni in water), at any point during electrolysis with Ni_3P or Ni_5P_4; this is in agreement with the stability of the CP analysis. In acid, we measured the released Ni concentration in the electrolyte during and following a break-in period (16 h). For the Ni_3P MPs, the amount of dissolved Ni increased to only 0.9 ± 0.4 wt % of the total catalyst content during the break-inperiod (0 to <16 h). After this stage, we did not observe further dissolution of Ni up to 48 h of continuous electrolysis (0.5 ± 0.4 wt %; see Figure S4 in the Supporting Information), in agreement with the CP analysis. Similarly, for the Ni_5P_4 MPs, Ni dissolution is minimal during the break-in period and no further dissolution is observed from 16 to 24 h of continuous electrolysis. These insignificant amounts of dissolved Ni are much smaller than those of Ni_2P NPs (pressed electrodes made without Nafion), for which 50% dissolution of Ni is observed after 16 h.[1,16] This minimal dissolution of surface atoms demonstrates the remarkable stability of Ni_3P MPs under catalytic conditions. The stability of Ni_3P contrasts with that of other high Ni

DOI: 10.1021/acscatal.7b04466
ACS Catal. 2018, 8, 4408−4419

Table 1. Electrocatalyst Performance in Acid (0.5 M H_2SO_4) and Alkali (1 M NaOH)[a]

	pH	Tafel slope (mV/dec)	j_0 (A/cm$^2_{geo}$)	$E(j = 10$ mA/cm$^2_{geo}$) (V vs RHE)	J (mA/cm$^2_{geo}$)		Faradaic efficiency (%)	Ni leached in 1st 16 h electrolysis (break-in) (%)	J (mA/cm$^2_{ECSA}$)		TOF at $\eta = 100$ mV (H_2/s)
					$\eta = 100$ mV	$\eta = 200$ mV			$\eta = 100$ mV	$\eta = 200$ mV	
Ni_3P MPs	0	41 ± 2	(3 ± 1) × 10^{-4}	−0.066	−26.6	−146.0	99 ± 16	0.9 ± 0.4	−0.049	−0.27	0.08 ± 0.02
Ni_3P MPs	14	119 ± 2	(5.2 ± 0.9) × 10^{-5}	−0.291	−0.5	−2.7	106 ± 12	0.01 ± 0.06	−9.2 × 10^{-4} [b]	−4.9 × 10^{-3} [b]	(1.4 ± 0.4) × 10^{-3} [b]
Ni_5P_4 MPs	0	30	5.8 × 10^{-4}	−0.043	−79.6	−264.8	100 ± 1[c]	14 ± 4[c]	−0.30	−0.99	0.5 ± 0.1
Ni_5P_4 MPs	14	121 ± 6	(2.9 ± 0.8) × 10^{-4}	−0.193	−3.3	−14.0	100 ± 5[c]	0.04 ± 4[c]	−1.2 × 10^{-2} [b]	−0.60[b]	(21 ± 5) × 10^{-3} [b]

[a]We include the details of turnover frequency (TOF) and electrochemical capacitance surface area (ECSA) estimations in the Supporting Information. [b]We assume that ECSA is the same in acid and base, and the uncertainty is the standard deviation for Ni_3P MPs. [c]Data for Ni_5P_4 nc-MP from ref 16.

content catalysts, e.g. NiMo nanoparticles (NPs), which readily dissolve during electrolysis in acid.[42] The instability of δ-NiMo can be attributed to its small enthalpy of formation, which is tiny (−0.51 kJ/mol at 700 °C)[43] in comparison to that of Ni_3P (−219.7 kJ/mol at STP).

We evaluated the potential dependence of Ni_3P HER activity using Tafel analysis (Table 1) over at last one decade of current density. Figure 2C plots current density vs overpotential for Ni_3P MPs/Nafion electrodes in acidic or alkaline solution. In acidic solution the Tafel region is restricted to the low-overpotential region, where only one active site is predicted by our DFT calculations (vide infra, Figure 4A). We note that at increased overpotentials numerous H adsorption sites are predicted to contribute to the electrochemical activity, but the evaluation of the reaction mechanism for these latter sites is beyond the scope of this work, as we focus on the closest to thermoneutral (most active) sites. The Tafel slope is 41 ± 2 mV/dec in acid and 119 ± 2 mV/dec in alkali. The exchange current density (j_0, x axis in Figure 2D) measures the intrinsic electron transfer rate between the catalyst and H^+(aq) at 0 V vs RHE: i.e., at zero electrochemical driving force. For Ni_3P, we find an exchange current density of $j_0 = (3 \pm 1) \times 10^{-4}$ A/cm$^2_{geo}$ in acid and (5.2 ± 0.9) × 10^{-5} A/cm$^2_{geo}$ in alkali.

DISCUSSION

Corrosion Stability and Bonding. First, we consider the chemical bonding in nickel phosphides. The increased stability of nickel phosphide compounds vs Ni(s) is quantified by the heat of formation of Ni_3P ($\Delta H_f = -220$ kJ/mol)[44] vs Ni(s) ($\Delta H_f = 0$ kJ/mol for STP), as shown in Figure 3A, which plots the negative of the enthalpy of formation per atom for each of the seven nickel phosphide compounds. Figure 3A reveals that the per-atom stability remains nearly constant as P content increases for Ni_3P, Ni_5P_2, $Ni_{12}P_5$, and Ni_2P, drops at P:Ni = 4:5, and drops still further above 2:1 in NiP_2 and NiP_3. The per-atom stability of the last compounds decreases by as much as 22% over the P-poor phases.

We calculated the electron localization function (ELF) by DFT.[45] It is a simple measure of electron localization which may be used to distinguish between different types of bonding: e.g., metallic, ionic, and covalent. The maximum ELF value of 1 corresponds to complete electron localization (shown as red regions in Figure 3B), whereas an ELF value equal to 0.5 corresponds to an ideal electron gas that is delocalized (green). We calculate the ELF in a plane coincident with two Ni−P bonds to show the extent of electron delocalization in Ni_3P. Most of the space between atoms is turquoise (ELF ≈ 0.46), indicating a delocalized electron cloud consistent with metallic bonding. This agrees with the metallic conductivity observed for Ni_3P (resistivity 4 × 10^{-6} Ω m). In addition to the major contribution from metallic bonding, there is partial charge transfer between Ni and P, suggesting that electrostatic interactions are important as well. Bader charge analysis yields a partial charge of +0.1 to +0.2 q_e on Ni and −0.2 to −0.3 q_e on P. This additional ionic contribution could explain the added stability of the nickel phosphide compounds over purely metallic bonding in Ni(s).

Next, we consider the effect of an applied potential on chemical stability. To determine which electronic states will be occupied upon electrochemical polarization, we calculate the Γ-point wave function at electronic energies of ∼−5 and ∼0.1 eV relative to the Fermi energy (E_F) (see Figure 3C). These energies were chosen as they correspond to energetically and

DOI: 10.1021/acscatal.7b04466
ACS Catal. 2018, 8, 4408−4419

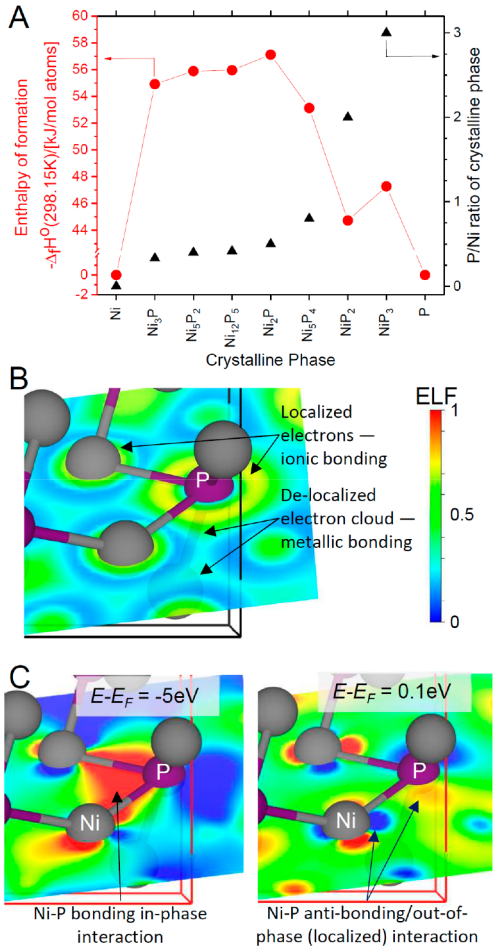

Figure 3. (A) (red) Enthalpy of formation per atom ($\Delta_f H°$) of bulk nickel phosphide phases. $\Delta_f H°$ is divided by the number of atoms per formula unit to allow a direct comparison between different bulk compositions. (black) P/Ni ratio of the crystalline phase. (B) Electron localization function for a plane coincident with two Ni−P bonds. The heat map indicates "localized electrons" in red (ELF ≈ 1) and "delocalized electrons" in green (ELF = 0.5) (ELF = 0 in blue). (C) Γ-point wave function along a Ni−P bond with the color map indicating the sign of the wave function (red, positive; blue, negative).

spatially overlapping P 3p and Ni 3d states (see the DOS in Figure S6 in the Supporting Information). The band at ∼0.1 eV vs E_F—analogous to the LUMO in molecular orbital bonding theory—represents the states that become filled first when the electrode is polarized during HER catalysis. The wave function projection shows lobes on Ni and P directed toward each other but of opposite sign: respectively (+) in red and (−) in blue. This state is therefore localized and antibonding in nature. The filling of antibonding states that occurs during electrode polarization weakens the Ni−P bonding interaction and increases the electron density on both atoms. The weaker Ni−P bonds and concomitant increase in electron density upon polarization create new adsorption sites for proton binding at these P atoms. As described below, the resulting adsorbed H atoms bind the most weakly of all H sites (near thermoneutral energy) and will therefore contribute the most to the high HER activity (vide infra). The projection at $E - E_F \approx -5$ eV shows an in-phase delocalized interaction between two Ni atoms and one P atom, indicating a delocalized metallic bond as predicted by the ELF above. In summary, mainly metallic bonding and some ionic bonding between Ni and P stabilize nickel phosphides in both acid and alkali. However, as is often the case in catalysis, bonds must be flexible to allow for efficient catalysis. Ni−P bonds are weakened at negatively biased potentials, shifting the H-binding energy of weak binding sites toward thermoneutrality—increasing the catalytic HER activity.

Finally, the 22% lower enthalpy of formation of NiP_2 in comparison to that of Ni_2P (Figure 3A) is likely a consequence of replacing stronger Ni−P metallic and ionic bonding with weaker P−P covalent interactions. Consistent with this trend, NiP_2 is known to be less corrosion resistant in air in comparison to the Ni-rich compounds—indicating a correlation between corrosion stability and enthalpy of formation for this pair of compounds.

Electrocatalytic Activity and Tafel Kinetics. Figure 2D plots the HER performance metrics of multiple transition-metal phosphides and sulfides in comparison to Ni_3P MPs at pH 0 using the data in Table 1. Ni_3P requires an overpotential of −0.066 V vs RHE to generate a stable current density of −10 mA/cm^2_{geo} for 16 h, comparable to that of Ni_5P_4 MPs and other top transition-metal phosphides (see Figure 2D). Industrial electrolyzers, however, operate at much greater current densities and, consequently, overpotentials. At 100 mV, Ni_3P is inferior to Ni_5P_4, the latter producing a 3 times higher current density in acid (Table 1).

Figure 2D shows that the Tafel slope of Ni_3P MPs in acid (41 ± 2 mV/dec) is larger than that of Ni_5P_4 (both as nc-MPs and MPs) but comparable to that of other top transition-metal phosphides (see Figure 2D).

This Tafel slope (TS) may be compared to the idealized HER reactions in acid in the low H coverage limit:[46]

Volmer step: $H^+(aq) + e^- \rightleftharpoons H^*$ TS 116

Heyrovsky step: $H^+(aq) + e^- + H^* \rightleftharpoons H_2(g)$ TS 38

Tafel step: $2H^* \rightleftharpoons H_2(g)$ TS 29

where H* represents H bound to the surface and slopes are in units of mV/dec. Experimental Tafel slopes, however, often deviate from these guideline values because they depend on H coverage.[47] The Tafel slope of Ni_5P_4 MPs and Pt in acid (∼30 mV/dec) indicates that the Tafel step is rate determining on Ni_5P_4. Ni_3P MPs, however, exhibit a Tafel slope of 41 mV/dec, which indicates that the Heyrovsky step is likely rate-determining. Since the Heyrovsky and Tafel steps involve one and two H*, respectively, we can infer that the H coverage on Ni_3P is smaller than that on Ni_5P_4 and Pt.

Finally, we find that the exchange current density in acid of Ni_3P MPs (Figure 2D) is 1 order of magnitude less than that of Ni_5P_4 nc-MPs and Pt but comparable to that of other top transition-metal phosphides such as Ni_2P NPs,[1] CoP NPs,[13] and $NiMoN_x/C$[48] (see Figure 2D). This can be explained by the low H* coverage on Ni_3P.

In alkali, Ni_3P MPs are corrosion free but require a higher overpotential (−0.291 V) to drive −10 mA/cm^2_{geo} than do Ni_5P_4 MPs (−0.193 V) (synthesized using the same solid-state method) and NiMo NPs (−0.082 V), a state of the art alkaline HER catalyst (but corrodes in acid).[42] At pH 14, the Tafel slope of Ni_3P MPs (119 ± 2 mV/dec) is near that of a polycrystalline Pt disk (98 mV/dec) (see the Supporting Information). Figure S2 compares the performance of Ni_3P MPs in alkali (pH 14) to that of benchmark electrocatalysts.

To investigate why these nickel phosphide catalysts perform worse in alkali than in acid, we excluded the effects of the

DOI: 10.1021/acscatal.7b04466
ACS Catal. 2018, 8, 4408−4419

Nafion binder by comparing CP analysis of Ni_5P_4 and Ni_3P MP electrodes both with and without Nafion. Figure S4A shows that there is no appreciable difference with and without Nafion in 1 M NaOH. Hence, the low geometric activity is likely due to the large particle size afforded by the high-temperature synthesis. By normalization to the estimated active electrochemical surface area, a more accurate comparison can be made to literature results (see the kinetic performance section below).

To explore the surface chemical state of the catalyst, XPS spectra were measured before and after 30 min of catalysis at −0.5 V vs RHE in 0.5 M H_2SO_4 and unavoidable air exposure during sample transfer. The resulting spectra (Ni and P 2p spectra, see Figures S10−S12) reveal the presence of a nickel phosphide reduced chemical state both before and after catalysis, as well as the presence of a layer ($\lesssim$1 nm thick) of nickel phosphorus oxides, $Ni_x(PO_y)_z$, formed by air exposure, comprised of a mixture of species (indistinguishable phosphate, phosphite, or hypophosphite) within the experimental fitting error (±0.2 eV; see the Supporting Information). It should be noted that the $Ni_x(PO_y)_z$ will be reduced under HER conditions, as has been observed by Raman spectroscopy for the $Co_x(PO_y)_z$ analogue.[49] This reduction is further supported by the induction period observed in the CP analysis in Figure 2A, which is significantly extended in alkali electrolyte, where the nickel phosphorus oxide is insoluble and will be fully reduced prior to reaching the catalytic steady state current, in agreement with the observations by ICP-OES analysis (see Figure S5). In contrast, in acid the phosphorus oxide partially dissolves (as seen by ICP-OES, see Figure S5) and the induction period is much shorter. As discussed above, in both acid and alkali no further change in Ni dissolution is observed after the break-in period, indicating catalyst stability.

Finally, survey spectra recorded of the Ni_3P MP catalyst after catalysis did not reveal any impurities other than residue from the electrolyte and epoxy from the electrode fabrication (Figure S14).

Surface Structure and Stability of $Ni_3P(001)$. The HER active site on transition-metal phosphides is debated in the literature. Most computational studies examine $Ni_2P(0001)$ surfaces, and none have considered the influence of surface reconstruction on the HER. The published DFT calculations of Ni_2P surfaces, which correspond to a single-crystal sample under ultrahigh vacuum (UHV), provide a point of comparison for our work here. There are two hypotheses for the HER active site on Ni_2P surfaces: (1) trigonal Ni_3-hollow and Ni−P bridge sites on $Ni_2P(0001)$[50] and (2) Ni−Ni bridge sites on low-index facets $Ni_2P(\bar{1}\bar{1}20)/(11\bar{2}1)$.[51] Single-crystal electrochemical studies would be necessary to possibly distinguish which of these hypotheses may be right. A recently published DFT study indicates that stable P-enriched reconstructions of $Ni_2P(0001)$ and $Ni_5P_4(0001)/(000\bar{1})$ can form under realistic synthesis conditions.[52] Little is known experimentally, however, about the surface structure and stability of Ni_3P. Ni_3P is predicted to have two possible terminations along the (001) plane: Ni_8 and Ni_4P_4. Hereafter, we label all surface reconstructions as "bulk layer composition"/"surface layer composition", e.g. $Ni_3P(s)/Ni_4P_4$.

We analyzed surface structure and thermodynamic stability using DFT calculations.[32−34] This approach reveals that three different (001) surface reconstructions form within the chemical potential range of Ni and P for which bulk $Ni_3P(s)$ is favored over other nickel phosphide stoichiometries and Ni(s): $Ni_3P(s)/Ni_4P_4$, $Ni_3P(s)/Ni_4P_4+V_{Ni}+P$, and $Ni_3P(s)/Ni_4P_4+2P$. These correspond respectively to a bulk termination, a reconstruction with one Ni vacancy (V_{Ni}) and one P adatom (P_{ad}), and a reconstruction with two P_{ad} adatoms. $Ni_3P(001)$ surface structure and stability depend on the Ni chemical potential during synthesis. For a detailed description of the surface phase diagram and atomic structures, see Figure S5.

Figure 4A shows the calculated differential free energy of H adsorption (ΔG_H) at U = 0 V vs RHE and pH 0. Figure 4B−D shows atomic representations of all the H* adsorption sites on each stable surface for different H coverages (n_H). ΔG_H at n_H = 1 differs substantially for $Ni_3P(s)/Ni_4P_4$ (−0.53 eV), $Ni_3P(s)/Ni_4P_4+V_{Ni}+P$ (−0.29 eV), and $Ni_3P(s)/Ni_4P_4+2P$ (−0.08). We define the maximum H coverage as the first value of n_H for which $\Delta G_H > 0$ (dotted black line in Figure 4A): i.e., H favors desorption as $H_2(g)$ over adsorption.

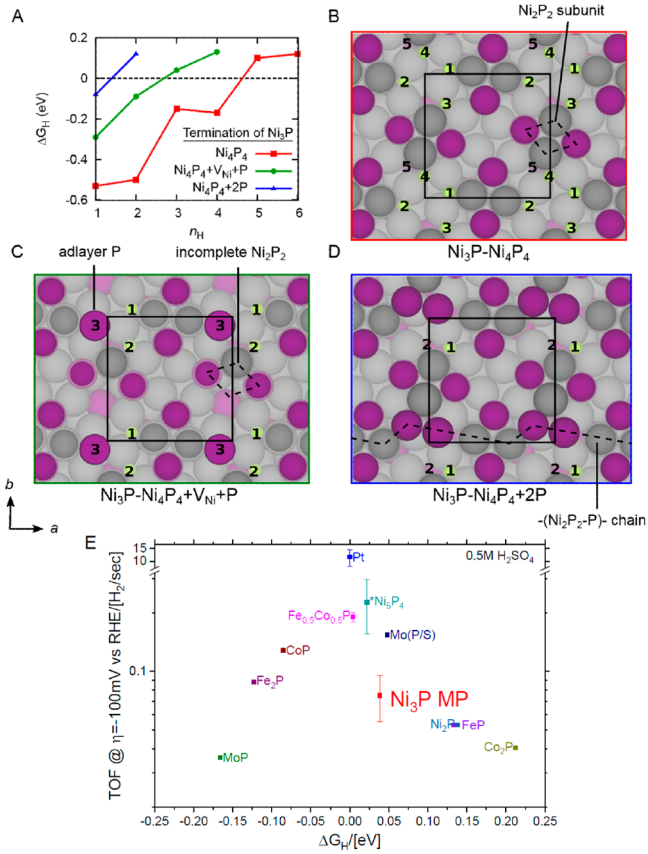

Figure 4. DFT calculations of H adsorption on stable stoichiometric and reconstructed $Ni_3P(001)$ surfaces. (A) H adsorption free energy as a function of H coverage (n_H) for the three stable $Ni_3P(001)$ surfaces at 0 V vs RHE and pH 0. H* sites (see numbers) on (B) $Ni_3P(s)/Ni_4P_4$, (C) $Ni_3P(s)/Ni_4P_4+V_{Ni}+P$, and (D) $Ni_3P(s)/Ni_4P_4+2P$. Dotted lines highlight the complete and incomplete Ni_2P_2 subunits and the −(Ni_2P_2−P)− chain. Ni, P, and H atoms are colored gray, purple, and lime green, respectively. Numbers on top of H atoms correspond to n_H. The H atom is not shown when $\Delta G_H(n_H) > 0$. (E) Electrochemical surface area (ECSA) derived TOF for Ni_3P MPs, Ni_5P_4 MPs, and Pt in comparison to values reported in ref 54. The asterisk (*) next to Ni_5P_4 in (E) indicates that the H-binding energy of Ni_5P_4 MPs is estimated on the basis of an electrochemical analysis (see the Supporting Information).

$Ni_3P(s)/Ni_4P_4$. Under Ni-rich conditions, formation of the stoichiometric $Ni_3P(s)/Ni_4P_4$ surface is thermodynamically

DOI: 10.1021/acscatal.7b04466
ACS Catal. 2018, 8, 4408−4419

preferred (see Figure S6 for the free energy vs composition). This surface is composed of repeating rhombus Ni_2P_2 subunits on a Ni subsurface (see Figure 4B). The equilibrium H coverage of this surface at 0 V vs RHE is four H atoms (labeled sites 1−4 in Figure 4B) bound at the distorted Ni_3-hollow sites formed by one surface Ni (in a Ni_2P_2 subunit) and two sublayer Ni atoms (the red line inFigure 4A plots ΔG_H from n_H = 1+ to 4+, i.e. low to maximum H coverage). The binding of a fifth H atom (labeled site 5 in Figure 4B) at a Ni_3-hollow adjacent to the fourth H has a limiting electrochemical potential of formation of 0.11 eV.

$Ni_3P(s)/Ni_4P_4+V_{Ni}+P$. At intermediate Ni chemical potentials, $Ni_3P(s)/Ni_4P_4$ is predicted to form a lower energy termination enriched with P through the formation of a nickel vacancy (V_{Ni}) and deposition of a P_{ad}, denoted $Ni_3P(s)/Ni_4P_4+V_{Ni}+P$. This reconstruction is generated by removing a Ni atom from one Ni_2P_2 subunit (see Figure 4B) and placing P between the remaining Ni of that subunit and the Ni of a neighboring, complete Ni_2P_2 subunit (see Figure 4C) in each unit cell. The P_{ad} sits directly above a Ni_3-hollow site in the subsurface layer, which stabilizes the P site.[52] At 0 V vs RHE, this surface binds two H atoms (labeled sites 1 and 2 in Figure 4C) at different Ni_3-hollow sites (green line in Figure 4A plots ΔG_H at n_H = 1+ to 2+). Binding of an additional H atop the P_{ad} (labeled site 3 in Figure 4C) has a limiting electrochemical potential of formation of 0.04 eV.

$Ni_3P(s)/Ni_4P_4+2P$. At the lowest Ni concentrations in the Ni_3P bulk stability region, the surface is predicted to favor the formation of the most P enriched termination $Ni_3P(s)/Ni_4P_4+2P$ (see Figure 4D). This termination can only bind one H (labeled site 1 in Figure 4D) in the absence of applied potential, while binding the second H atom (site 2) requires 0.12 eV to form (blue line in Figure 4A plots ΔG_H from n_H = 1+).

In general, H prefers strong adsorption at distorted Ni_3-hollow sites. Since the experimental synthesis is Ni-rich (recall that excess Ni(s) must be removed), $Ni_3P(s)/Ni_4P_4+2P$ is unlikely to form and so we dismiss it from further consideration. Decreasing the Ni chemical potential (by increasing its concentration) gives $Ni_3P(s)/Ni_4P_4+V_{Ni}+P$, which decreases the H coverage at 0 V vs RHE from 4 (high $\Delta\mu_{Ni}$) to 2 (intermediate $\Delta\mu_{Ni}$) (Figure 4A, red vs green traces). This agrees with our experimental prediction of lower H coverage on $Ni_3P(001)$ from the exchange current density at zero applied potential. Under reducing potentials, however, the P_{ad} of $Ni_3P(s)/Ni_4P_4+V_{Ni}+P$ provides nearly thermoneutral H binding, ideal for the HER.

HER Mechanism on $Ni_3P(001)$ Surfaces. First, we discuss the H adsorption energetics of the stable, experimentally relevant $Ni_3P(001)$ surfaces. Figure 4A shows that ΔG_H increases (i.e., H adsorption weakens) by 0.13−0.14 eV per additional H* on $Ni_3P(s)/Ni_4P_4$ and $Ni_3P(s)/Ni_4P_4+V_{Ni}+P$. Our calculations also reveal that ΔG_H increases as the mole fraction of P at the surface increases, relative to that of the bulk composition. This can be explained by the electrostatic repulsion between the negatively charged hydride and phosphide species.

For n_H = 1, the average Löwdin charge of H* is −0.26 q_e across all stable $Ni_3P(001)$ surfaces. There are two different charges of surface P within an individual Ni_2P_2 subunit: −0.66 and −0.76 q_e. However, when the Ni_2P_2 subunit has a V_{Ni}, as in the case of $Ni_3P(s)/Ni_4P_4+V_{Ni}+P$, the charge of both surface P atoms is −0.65 q_e. The charge of the P_{ad} on $Ni_3P(s)/Ni_4P_4+V_{Ni}+P$ ranges from −0.39 to −0.46 q_e. Thus, P enrichment decreases the repulsion between H* and surface P, at the P_{ad} site. Weakened repulsion between H and P is evident from the order of occupation of the H binding sites. For $Ni_3P(s)/Ni_4P_4$, H binds exclusively to Ni. However, as the surface P concentration increases, P_{ad} forms that weakly binds H, thereby generating a highly active site for the HER (see n_H = 3 for the green line in Figure 4A and site 3 in Figure 4C).

ΔG_H is frequently used as a descriptor of HER activity.[53] This approach was recently expanded to bulk-derived terminations of various transition-metal phosphides.[54] This type of DFT analysis is based on the Sabatier principle, which states that the interaction between the catalyst and adsorption should be neither too strong nor too weak. In other words, optimal HER requires a ΔG_H value of 0 eV at 0 V vs RHE. With this definition, the ΔG_H value closest to 0 eV is the descriptor of a catalyst's HER activity, as this is the most kinetically labile H*. Using this descriptor approach, a solid solution of CoP and FeP ($Fe_{0.5}Co_{0.5}P$) was identified as having the most ideal ΔG_H (0.004 eV) among other transition-metal phosphides.[54] This work, however, does not take into account the possibility of new active sites forming at higher overpotentials, which is highly relevant for kinetic studies. We find that all three stable surfaces of $Ni_3P(001)$ provide competitive ΔG_H values at 0 V vs RHE, ranging from −0.17 to −0.08 eV.

Because HER current is generally very low for transition-metal phosphides until a threshold potential is reached, we consider the additional H* sites formed at low overpotentials (η < 0.1 V) as the precursors to H_2 formation. For $Ni_3P(001)$, the application of a small reducing potential (−0.040 V) accesses a new, kinetically labile H* site on $Ni_3P(s)/Ni_4P_4+V_{Ni}+P$ directly atop the P_{ad} (see site 3 in Figure 4D) by shifting the H binding energy toward thermoneutrality.

Identifying the Active Surface Reconstruction of Ni_3P. We find that a small potential of −0.038 V vs RHE drives a significant HER current density of < −3 mA/cm^2_{geo} at pH = 0. This is consistent with the P_{ad} active site on $Ni_3P(s)/Ni_4P_4+V_{Ni}+P$, which requires −0.04 V for thermoneutral H adsorption (see site 3 in Figure 4C). On the other hand, $Ni_3P(s)/Ni_4P_4$, which has a higher surface Ni content, requires a more reducing potential (−0.100 V vs RHE) for thermoneutral H adsorption, thus establishing this termination as a less likely source of $H_2(g)$ at low overpotentials.

Finally, we consider the observed Tafel slope. Since H* at the P_{ad} site of $Ni_3P(s)/Ni_4P_4+V_{Ni}+P$ (see site 3 in Figure 4C) is surrounded by strongly bound H* at Ni_3-hollow sites (sites 1 and 2 in Figure 4C), the HER on $Ni_3P(001)$ likely does not follow the Volmer−Tafel mechanism. Instead, our calculations suggest that $Ni_3P(001)$ favors the Volmer−Heyrovsky mechanism in acid (i.e., direct hydride abstraction by a proton), which agrees with our experimentally determined Tafel slope (41 mV/dec). We include the ΔG_H for H at the P_{ad} site of $Ni_3P(s)/Ni_4P_4+V_{Ni}+P$ in the volcano plot in Figure 4E, together with the benchmark transition metal phosphide catalysts reported in ref 54. The Volmer−Heyrovsky mechanism observed on Ni_3P is also reported for Ni_2P (Tafel slope 38−46 mV/dec[1,16]) which has a characteristic ΔG_H value of 0.14 eV[54,55] and is therefore farther to the right (indicating more weakly bound H*) in Figure 4E.[55] The mechanism on these two weakly binding catalysts is in contrast to the mechanism on Pt and Ni_5P_4 that is observed experimentally to favor the Volmer−Tafel mechanism as seen by the Tafel slopes of 29 and 31−33 mV/dec, respectively.[16,56] It is thus clear that

DOI: 10.1021/acscatal.7b04466
ACS Catal. 2018, 8, 4408−4419

the volcano type behavior previously reported for pure metals[57] and several transition-metal phosphides[54] also applies to these nickel phosphides. Furthermore, we observe that weakly binding transition-metal phosphides correlates with a preferred Volmer–Heyrovsky HER mechanism, whereas the moderately binding Ni_5P_4 and Pt follow the Volmer–Tafel mechanism. Thus, to achieve the most highly active catalysts, at the very peak of the volcano curve, the catalyst has to be designed with a ΔG_H value near that of Pt (0 eV), which therefore will observe the Volmer–Tafel mechanism.

We emphasize that, at high applied overpotentials, other weakly binding H* species (at Ni and Ni–Ni bridging sites, both dimers and hollows) can contribute to the overall activity. However, this would likely change the rate-determining step of HER (from Heyrovsky to Volmer) and the observed Tafel slope (from ∼40 mV/dec to ∼120 mV/dec). To test the dependence of HER activity on the presence of surface P species, the Ni sites were selectively poisoned with KSCN, leaving only P sites available for H adsorption. To ensure complete Ni poisoning, 2 equiv of KSCN was added per surface site (combined Ni and P) to the electrolyte during CP analysis at −10 mA/cm^2_{geo} (optical spectroscopy confirmed SCN^- binding to the catalyst; see Figure S16). Figure S17 shows the effect of SCN^- on the Ni_3P and Ni_5P_4 MP catalysts during the CP measurement. Over the course of 25 h, the overpotential slowly increases to a slightly higher steady state by only 17 and 7 mV for Ni_3P and Ni_5P_4 MPs, respectively. The Tafel slope before and after poisoning and therefore the rate-determining step are found to be unchanged (see Figures S17 and S18). This experiment strongly indicates that the most active HER sites are P-based and not Ni-based on both catalysts. Figure 4B–D shows that the unreconstructed, bulk-terminated $Ni_3P(001)$ surface only contains Ni-based sites. Indeed, of the most stable surface terminations and reconstructions considered here, only the $Ni_3P(s)/Ni_4P_4+V_{Ni}+P$ reconstruction shows P-based H-binding sites. We conclude that both experiments and theory support the prediction that surface P sites are the active sites for HER electrocatalysis.

Kinetic Performance and Comparisons. To compare the electrochemical activity of Ni_3P MPs with that of other top transition-metal phosphides,[54] we estimate the electrochemical surface area (ECSA) and turnover frequency (TOF). We determine ECSA using the capacitive charge estimation in a potential range (−0.1 to 0 V vs RHE) where surface oxidation is unlikely to occur (for details, see the Supporting Information). We find that the surface area of Ni_3P (546 ± 36% cm^2_{ECSA}/cm^2_{geo}) is 48.8 times larger than that of CoP thin films (11.2 cm^2_{ECSA}/cm^2_{geo}).[58] The surface area of the MPs agrees with our previous study of porous pellet electrodes on the same order of magnitude as the estimated total catalyst surface area from BET, calculated as a catalyst loading of 177 mg_{cat}/cm^2_{geo} × 1100 cm^2_{BET}/g_{cat} = 195 cm^2_{BET}/cm^2_{geo}.[16] We note that, while there are uncertainties in the ECSA surface area estimate (associated with the unknown surface charge per area, surface adsorbates, etc.), this is the best available method and allows direct comparison to literature values for transition-metal phosphides.[54,58] It should be noted that the use of the ECSA surface area estimate corresponds to the most conservative determination of the turnover frequency (TOF). We also find that the active surface area normalized current for Ni_3P MPs (−0.049 ± 0.015 mA/cm^2_{ECSA} at −0.100 V) is smaller than that of Ni_5P_4 MPs (−0.30 mA/cm^2_{ECSA}) but comparable to that of other top transition-metal phosphides such as $Fe_{0.5}Co_{0.5}P$ (−0.13 mA/cm^2_{ECSA}) and CoP (−0.073 mA/cm^2_{ECSA}).[54] The surface area and normalized current of Ni_3P MPs are clearly among those of state of the art HER catalysts.

We estimate TOF from the ECSA-normalized current and assume an equal distribution of surface Ni and P active sites.[1,16,54] The estimation of TOF introduces several crude approximations that result in fairly large variations even for the same material: e.g., determination of the ECSA alone can easily vary by 4-fold for similar carbon samples.[59] Figure 4E shows the estimated TOF of Ni_3P MPs (0.08 s^{-1} at η = 100 mV and pH 0) is ∼6 times smaller than that of Ni_5P_4 MPs (0.5 s^{-1}). The latter TOF is 6-fold smaller than for nanocrystalline particles of Ni_5P_4 nc-MPs (3.5 s^{-1});[16] the discrepancy is likely due to the different methods utilized to estimate the active surface area. The estimated TOF reveals that Ni_3P MPs exhibit good HER activity on a per-site basis. The TOF of Pt foil (11.5 s^{-1}), however, is more than 1 order of magnitude higher than that of the second-best transition-metal phosphide catalyst (Ni_5P_4).[16]

In alkaline media, the estimated TOF of Ni_3P is 0.001 s^{-1} (at η = 100 mV),[16] which is comparable to that previously determined for a Ni_2P nanoparticle catalyst in 1 M NaOH (0.004 s^{-1} at η = 100 mV),[16] another highly active HER catalyst. Still, these TOFs are ∼2 orders of magnitude lower than those of the state of the art non-noble-metal HER catalysts Mo_2C (0.15 s^{-1} at η = 100 mV)[60] and Ni_5P_4 nc-MPs (0.79 s^{-1} at η = 100 mV).[16] For reference, the TOFs of noble-metal-free catalysts are 1 order of magnitude lower than those of noble-metal catalysts: e.g., benchmark Pt (3.6 s^{-1} at η = 100 mV)[16] and the laboratory state of the art Ru/C_2N catalyst (1.66 s^{-1} at η = 50 mV).[3] For Ni_3P, lower activity in alkali in comparison to acid suggests that the thermodynamics of HER on the P adlayer are non-Nernstian with respect to changes in pH. That is, the shift of one pH unit does not result in the expected ∼59 mV shift in potential to achieve the same current density. Non-Nernstian behavior is also indicated by the change in the Tafel slope from 41 mV/dec in acid to 119 mV/dec in base. The significant Tafel slope change corresponds to a change in the rate-determining step from a Heyrovsky-type step to a Volmer-type step: i.e., proton adsorption has become rate limiting. The origin of this non-Nernstian behavior could be due to surface passivation by P–OH formation, pH effects on the electrochemical double layer, or different reconstructions being stable at high pH.

We will briefly comment on the assumptions made in our TOF calculation. Again, we assume an equal number of evenly distributed Ni and P surface active sites. This assumption places a lower bound on the TOF of transition-metal phosphide catalysts with a lower density of active sites, which is the case for $Ni_3P(001)$ as shown by our DFT calculations above (see Figure 4E). The conservative geometric estimate of the surface-active site density is 2.02 × 10^{15} sites/cm^2. Using DFT calculations, however, the surface-active site density of Ni = $P(s)/Ni_4P_4+V_{Ni}+P$ is 6.24 × 10^{14} sites/cm^2 (see the Supporting Information). Therefore, the TOF of transition-metal phosphide catalysts may be ∼1 order of magnitude larger than those previously reported even in a conservative estimate, nearly bridging the gap between Pt and other top transition-metal phosphide catalysts.

CONCLUSIONS

Ni_3P was previously dismissed as an HER catalyst due to its low activity when it was formed from amorphous precursors and

DOI: 10.1021/acscatal.7b04466
ACS Catal. 2018, 8, 4408–4419

tested in alkaline solution and its anticipated low stability in acid by analogy to Ni(*s*) electrodes. We show that such an extrapolation is incorrect, as it fails to consider the added influence of ionic Ni−P bonding. This additional bonding contribution is the source of its larger heat of formation vs Ni(*s*) and high corrosion stability. Taken together, the high intrinsic HER activity of Ni_3P MPs (comparable to that of other top transition-metal phosphides), its excellent corrosion stability under HER conditions in both strong acid and base, and low-cost synthesis may allow this material to substitute for both Pt-group metals in large-scale acid electrolysis and for Ni electrodes in alkaline electrolysis. Using DFT calculations, we find that a P-enriched (001) surface of Ni_3P is most active for the HER. At low overpotentials we identify the active site as a P adatom (P_{ad}) that forms during reconstruction and provides nearly thermoneutral H binding ($\Delta G_H \approx 0.04$ eV). A previously proposed HER active site on $Ni_2P(0001)$, i.e. the Ni_3 hollow site,[50] is present on $Ni_3P(001)$ but binds a P_{ad} during reconstruction. This P_{ad} reconstruction is similar to the reconstructions observed on $Ni_2P(0001)$ and $Ni_5P_4(0001)$ under vacuum, as previously proposed by Wexler et al.[52] The structure difference between Ni-rich Ni_3P and P-rich Ni_2P and Ni_5P_4 causes a change in bonding geometry of the Ni_3-hollow, in turn leading to a variation in ΔG_H and the catalyst's corresponding HER activity. We further demonstrate a correlation of the proposed rate-determining step (Tafel vs Heyrovsky) and the ΔG_H binding energy for a series of three nickel phosphides. The insight into the active site geometry on $Ni_3P(001)$ presented here and its similarity to that of other nickel phosphides suggests that this could serve as a general design principle for the development of novel transition-metal phosphide catalysts with even higher activity and thus provide a structural motif for further climbing the HER volcano plot. DFT calculations are shown to be a powerful tool to predict reconstruction of energy-minimized surfaces, which is invaluable to an atomic level understanding of catalysis. The insight into the active site geometry on $Ni_3P(001)$ presented here and its similarity to other nickel phosphides suggests that this could serve as a general design principle for the development of novel transition-metal phosphide catalysts with even higher activity and thus provide a structural motif for further climbing the HER volcano plot.

■ ASSOCIATED CONTENT

Supporting Information

The Supporting Information is available free of charge on the ACS Publications website at DOI: 10.1021/acscatal.7b04466.

Experimental details, density of states, and ICP-OES and other data (PDF)

■ AUTHOR INFORMATION

Corresponding Authors

*E-mail for M.G.: martha@chem.rutgers.edu.
*E-mail for A.M.R.: rappe@sas.upenn.edu.
*E-mail for G.C.D.: dismukes@chem.rutgers.edu.

ORCID

Anders B. Laursen: 0000-0002-1386-9202
Robert B. Wexler: 0000-0002-6861-6421
Jing Li: 0000-0001-7792-4322
Martha Greenblatt: 0000-0002-1806-2766
Andrew M. Rappe: 0000-0003-4620-6496
G. Charles Dismukes: 0000-0003-0155-0541

Notes

The authors declare no competing financial interest.

■ ACKNOWLEDGMENTS

Research at Rutgers was jointly funded by the National Science Foundation, Division of Chemical, Bioengineering, Environmental, and Transport Systems (CBET), and the U.S. Department of Energy, Office of Energy Efficiency and Renewable Energy, Fuel Cell Technologies Office, award number CBET-1433492. A.B.L. thanks Rutgers University for fellowship support. Research at Penn was supported by the Department of Energy, Division of Basic Energy Sciences, award number DE-FG02-07ER15920. The authors also acknowledge computational support from the High-Performance Computing Modernization Office and the National Energy Research Scientific Computing Center.

■ ABBREVIATIONS

DFT,density functional theory; HER,hydrogen evolution reaction; MPs,microparticles; TOF,turnover frequency.

■ REFERENCES

(1) Popczun, E. J.; McKone, J. R.; Read, C. G.; Biacchi, A. J.; Wiltrout, A. M.; Lewis, N. S.; Schaak, R. E. Nanostructured nickel phosphide as an electrocatalyst for the hydrogen evolution reaction. *J. Am. Chem. Soc.* **2013**, *135*, 9267−9270.

(2) Chen, Z.; Jaramillo, T. F.; Deutsch, T. G.; Kleiman-Shwarsctein, A.; Forman, A. J.; Gaillard, N.; Garland, R.; Takanabe, K.; Heske, C.; Sunkara, M.; McFarland, E. W.; Domen, K.; Miller, E. L.; Turner, J. A.; Dinh, H. N. Accelerating materials development for photoelectrochemical hydrogen production: Standards for methods, definitions, and reporting protocols. *J. Mater. Res.* **2010**, *25*, 3−16.

(3) Mahmood, J.; Li, F.; Jung, S.-M.; Okyay, M. S.; Ahmad, I.; Kim, S.-J.; Park, N.; Jeong, H. Y.; Baek, J.-B. An efficient and pH-universal ruthenium-based catalyst for the hydrogen evolution reaction. *Nat. Nanotechnol.* **2017**, *12*, 441−446.

(4) Vesborg, P. C. K.; Jaramillo, T. F. Addressing the terawatt challenge: scalability in the supply of chemical elements for renewable energy. *RSC Adv.* **2012**, *2*, 7933−7947.

(5) Cao, B.; Veith, G. M.; Neuefeind, J. C.; Adzic, R. R.; Khalifah, P. G. Mixed close-packed cobalt molybdenum nitrides as non-noble metal electrocatalysts for the hydrogen evolution reaction. *J. Am. Chem. Soc.* **2013**, *135*, 19186−19192.

(6) Li, Y.; Wang, H.; Xie, L.; Liang, Y.; Hong, G.; Dai, H. MoS_2 nanoparticles grown on graphene: An advanced catalyst for the hydrogen evolution reaction. *J. Am. Chem. Soc.* **2011**, *133*, 7296−7299.

(7) Lukowski, M. A.; Daniel, A. S.; Meng, F.; Forticaux, A.; Li, L.; Jin, S. Enhanced hydrogen evolution catalysis from chemically exfoliated metallic MoS_2 nanosheets. *J. Am. Chem. Soc.* **2013**, *135*, 10274−10277.

(8) Hinnemann, B.; Moses, P. G.; Bonde, J.; Jørgensen, K. P.; Nielsen, J. H.; Horch, S.; Chorkendorff, I.; Nørskov, J. K. Biomimetic hydrogen evolution: MoS_2 nanoparticles as catalyst for hydrogen evolution. *J. Am. Chem. Soc.* **2005**, *127*, 5308−5309.

(9) Jaramillo, T. F.; Jørgensen, K. P.; Bonde, J.; Nielsen, J. H.; Horch, S.; Chorkendorff, I. Identification of active edge sites for electrochemical H_2 evolution from MoS_2 nanocatalysts. *Science* **2007**, *317*, 100−102.

(10) Laursen, A. B.; Vesborg, P. C. K.; Chorkendorff, I. A high-porosity carbon molybdenum sulphide composite with enhanced electrochemical hydrogen evolution and stability. *Chem. Commun.* **2013**, *49*, 4965−4967.

(11) Laursen, A. B.; Kegnæs, S.; Dahl, S.; Chorkendorff, I. Molybdenum sulfides—efficient and viable materials for electro - and photoelectrocatalytic hydrogen evolution. *Energy Environ. Sci.* **2012**, *5*, 5577−5591.

DOI: 10.1021/acscatal.7b04466
ACS Catal. 2018, 8, 4408−4419

(12) Wang, J.; Zhong, H.; Wang, Z.; Meng, F.; Zhang, X. Integrated Three-Dimensional Carbon Paper/Carbon Tubes/Cobalt-Sulfide Sheets as an Efficient Electrode for Overall Water Splitting. *ACS Nano* **2016**, *10*, 2342−2348.
(13) Popczun, E. J.; Read, C. G.; Roske, C. W.; Lewis, N. S.; Schaak, R. E. Highly active electrocatalysis of the hydrogen evolution reaction by cobalt phosphide nanoparticles. *Angew. Chem., Int. Ed.* **2014**, *53*, 5427−5430.
(14) Callejas, J. F.; McEnaney, J. M.; Read, C. G.; Crompton, J. C.; Biacchi, A. J.; Popczun, E. J.; Gordon, T. R.; Lewis, N. S.; Schaak, R. E. Electrocatalytic and photocatalytic hydrogen production from acidic and neutral-pH aqueous solutions using iron phosphide nanoparticles. *ACS Nano* **2014**, *8*, 11101−11107.
(15) McEnaney, J. M.; Chance Crompton, J.; Callejas, J. F.; Popczun, E. J.; Biacchi, A. J.; Lewis, N. S.; Schaak, R. E. Amorphous molybdenum phosphide nanoparticles for electrocatalytic hydrogen evolution. *Chem. Mater.* **2014**, *26*, 4826−4831.
(16) Laursen, A. B.; Patraju, K. R.; Whitaker, M. J.; Retuerto, M.; Sarkar, T.; Yao, N.; Ramanujachary, K. V.; Greenblatt, M.; Dismukes, G. C. Dismukes, Nanocrystalline Ni_5P_4: a hydrogen evolution electrocatalyst of exceptional efficiency in both alkaline and acidic media. *Energy Environ. Sci.* **2015**, *8*, 1027−1034.
(17) Wang, Z.-L.; Hao, X.-F.; Jiang, Z.; Sun, X.-P.; Xu, D.; Wang, J.; Zhong, H.-X.; Meng, F.-L.; Zhang, X.-B. C and N hybrid coordination derived Co−C−N complex as a highly efficient electrocatalyst for hydrogen evolution reaction. *J. Am. Chem. Soc.* **2015**, *137*, 15070−15073.
(18) Merki, D.; Fierro, S.; Vrubel, H.; Hu, X. Amorphous molybdenum sulfide films as catalysts for electrochemical hydrogen production in water. *Chem. Sci.* **2011**, *2*, 1262.
(19) Aso, K.; Hayashi, A.; Tatsumisago, M. Phase-selective synthesis of nickel phosphide in high-boiling solvent for all-solid-state lithium secondary batteries. *Inorg. Chem.* **2011**, *50*, 10820−10824.
(20) Jin, L.; Xia, H.; Huang, Z.; Lv, C.; Wang, J.; Humphrey, M. G.; Zhang, C. Phase separation synthesis of trinickel monophosphide porous hollow nanospheres for efficient hydrogen evolution. *J. Mater. Chem. A* **2016**, *4*, 10925−10932.
(21) Huang, Z.; Chen, Z.; Chen, Z.; Lv, C.; Meng, H.; Zhang, C. $Ni_{12}P_5$ nanoparticles as an efficient catalyst for hydrogen generation via electrolysis and photoelectrolysis. *ACS Nano* **2014**, *8*, 8121−8129.
(22) Feng, L.; Vrubel, H.; Bensimon, M.; Hu, X. Easily-prepared dinickel phosphide (Ni_2P) nanoparticles as an efficient and robust electrocatalyst for hydrogen evolution. *Phys. Chem. Chem. Phys.* **2014**, *16*, 5917−5921.
(23) Cao, S.; Chen, Y.; Wang, C.-J.; He, P.; Fu, W.-F. Highly efficient photocatalytic hydrogen evolution by nickel phosphide nanoparticles from aqueous solution. *Chem. Commun.* **2014**, *50*, 10427.
(24) Pan, Y.; Liu, Y.; Zhao, J.; Yang, K.; Liang, J.; Liu, D.; Hu, W.; Liu, D.; Liu, Y.; Liu, C. Monodispersed nickel phosphide nanocrystals with different phases: synthesis, characterization and electrocatalytic properties for hydrogen evolution. *J. Mater. Chem. A* **2015**, *3*, 1656−1665.
(25) Jiang, P.; Liu, Q.; Sun, X. NiP_2 nanosheet arrays supported on carbon cloth: an efficient 3D hydrogen evolution cathode in both acidic and alkaline solutions. *Nanoscale* **2014**, *6*, 13440−13445.
(26) Pourbaix, M. *Atlas of Electrochemical Equilibria in Aqueous Solutions, Version 2*, 2nd ed.; National Association of Corrosion Engineers: Houston, TX, 1974.
(27) Mund, K.; Richter, G.; Schulte, R.; Von Sturm, F. Electrocatalysis on phosphides of iron group metals and ternary compounds. *Ber. Bunsen-Ges.* **1973**, *77*, 839−842.
(28) Kucernak, A. R. J.; Naranammalpuram Sundaram, V. N. Nickel phosphide: the effect of phosphorus content on hydrogen evolution activity and corrosion resistance in acidic medium. *J. Mater. Chem. A* **2014**, *2*, 17435−17445.
(29) Burchardt, T.; Hansen, V.; Våland, T. Microstructure and catalytic activity towards the hydrogen evolution reaction of electrodeposited NiP_x alloys. *Electrochim. Acta* **2001**, *46*, 2761−2766.
(30) Burchardt, T. The effect of deposition temperature on the catalytic activity of Ni-P alloys toward the hydrogen reaction. *Int. J. Hydrogen Energy* **2002**, *27*, 323−328.
(31) Hajizamani, M.; Alizadeh, A.; Ehsani, N. Deposition of a Ni_3P nano-scale layer on B_4C nanoparticles by simple electroless plating in an acidic bath. *Appl. Nanosci.* **2012**, *2*, 417−421.
(32) Rajagopal, A. K.; Callaway, J. Inhomogeneous Electron Gas. *Phys. Rev. B* **1973**, *7*, 1912−1919.
(33) Kohn, W.; Sham, L. J. Self-consistent equations including exchange and correlation effects. *Phys. Rev.* **1965**, *140*, A1133−A1138.
(34) Giannozzi, P.; Baroni, S.; Bonini, N.; Calandra, M.; Car, R.; Cavazzoni, C.; Ceresoli, D.; Chiarotti, G. L.; Cococcioni, M.; Dabo, I.; Dal Corso, A.; de Gironcoli, S.; Fabris, S.; Fratesi, G.; Gebauer, R.; Gerstmann, U.; Gougoussis, C.; Kokalj, A.; Lazzeri, M.; Martin-Samos, L.; Marzari, N.; Mauri, F.; Mazzarello, R.; Paolini, S.; Pasquarello, A.; Paulatto, L.; Sbraccia, C.; Scandolo, S.; Sclauzero, G.; Seitsonen, A. P.; Smogunov, A.; Umari, P.; Wentzcovitch, R. M. QUANTUM ESPRESSO: a modular and open-source software project for quantum simulations of materials. *J. Phys.: Condens. Matter* **2009**, *21*, 395502.
(35) Rappe, A. M.; Rabe, K. M.; Kaxiras, E.; Joannopoulos, J. D. Optimized pseudopotentials. *Phys. Rev. B: Condens. Matter Mater. Phys.* **1990**, *41*, 1227−1230.
(36) Ramer, N. J.; Rappe, A. M. Designed nonlocal pseudopotentials for enhanced transferability. *Phys. Rev. B: Condens. Matter Mater. Phys.* **1999**, *59*, 12471.
(37) *Opium - pseudopotential generator*, 2009; http://opium.sourceforge.net (accessed July 19, 2016).
(38) Perdew, J. P.; Burke, K.; Ernzerhof, M. Generalized Gradient Approximation Made Simple. *Phys. Rev. Lett.* **1996**, *77*, 3865−3868.
(39) Grimme, S. Semiempirical GGA-type density functional constructed with a long-range dispersion correction. *J. Comput. Chem.* **2006**, *27*, 1787−1799.
(40) Barone, V.; Casarin, M.; Forrer, D.; Pavone, M.; Sambi, M.; Vittadini, A. Role and effective treatment of dispersive forces in materials: Polyethylene and graphite crystals as test cases. *J. Comput. Chem.* **2009**, *30*, 934−939.
(41) Zelinska, M.; Oryshchyn, S.; Zhak, O.; Pivan, J. Y.; Potel, M.; Noël, H. Redetermination of Ni_5P_4. *Acta Crystallogr., Sect. E: Struct. Rep. Online* **2007**, *63*, i158−i159.
(42) McKone, J. R.; Sadtler, B. F.; Werlang, C. A.; Lewis, N. S.; Gray, H. B. Ni-Mo nanopowders for efficient electrochemical hydrogen evolution. *ACS Catal.* **2013**, *3*, 166−169.
(43) Wang, Y.; Woodward, C.; Zhou, S. H.; Liu, Z.-K.; Chen, L.-Q. Structural stability of Ni−Mo compounds from first-principles calculations. *Scr. Mater.* **2005**, *52*, 17−20.
(44) Gordienko, S. P. Enthalpies of formation and atomization for iron-group metal phosphides. *Powder Metall. Met. Ceram.* **1996**, *34*, 544−547.
(45) Becke, A. D.; Edgecombe, K. E. A simple measure of electron localization in atomic and molecular systems. *J. Chem. Phys.* **1990**, *92*, 5397−5403.
(46) Thomas, J. G. N. Kinetics of electrolytic hydrogen evolution and the adsorption of hydrogen by metals. *Trans. Faraday Soc.* **1961**, *57*, 1603.
(47) Shinagawa, T.; Garcia-Esparza, A. T.; Takanabe, K. Insight on Tafel slopes from a microkinetic analysis of aqueous electrocatalysis for energy conversion. *Sci. Rep.* **2015**, *5*, 13801−13822.
(48) Chen, W. F.; Sasaki, K.; Ma, C.; Frenkel, A. I.; Marinkovic, N.; Muckerman, J. T.; Zhu, Y.; Adzic, R. R. Hydrogen-evolution catalysts based on non-noble metal nickel-molybdenum nitride nanosheets. *Angew. Chem., Int. Ed.* **2012**, *51*, 6131−6135.
(49) Saadi, F. H.; Carim, A. I.; Verlage, E.; Hemminger, J. C.; Lewis, N. S.; Soriaga, M. P. CoP as an acid-stable active electrocatalyst for the hydrogen-evolution reaction: Electrochemical synthesis, interfacial characterization and performance evaluation. *J. Phys. Chem. C* **2014**, *118*, 29294−29300.
(50) Liu, P.; Rodriguez, J. A. Catalysts for hydrogen evolution from the [NiFe] hydrogenase to the $Ni_2P(001)$ surface: The importance of ensemble effect. *J. Am. Chem. Soc.* **2005**, *127*, 14871−14878.

DOI: 10.1021/acscatal.7b04466
ACS Catal. 2018, 8, 4408−4419

(51) Hansen, M. H.; Stern, L.-A.; Feng, L.; Rossmeisl, J.; Hu, X. Widely available active sites on Ni_2P for electrochemical hydrogen evolution – insights from first principles calculations. *Phys. Chem. Chem. Phys.* **2015**, *17*, 10823−10829.
(52) Wexler, R. B.; Martirez, J. M. P.; Rappe, A. M. Stable Phosphorus-Enriched (0001) Surfaces of Nickel Phosphides. *Chem. Mater.* **2016**, *28*, 5365−5372.
(53) Skúlason, E.; Tripkovic, V.; Björketun, M. E.; Gudmundsdóttir, S.; Karlberg, G.; Rossmeisl, J.; Bligaard, T.; Jónsson, H.; Nørskov, J. K. Modeling the Electrochemical Hydrogen Oxidation and Evolution Reactions on the Basis of Density Functional Theory Calculations. *J. Phys. Chem. C* **2010**, *114*, 18182−18197.
(54) Kibsgaard, J.; Tsai, C.; Chan, K.; Benck, J. D.; Nørskov, J. K.; Abild-Pedersen, F.; Jaramillo, T. F. Designing an improved transition metal phosphide catalyst for hydrogen evolution using experimental and theoretical trends. *Energy Environ. Sci.* **2015**, *8*, 3022−3029.
(55) Wexler, R. B.; Martirez, J. M. P.; Rappe, A. M. Active Role of Phosphorus in the Hydrogen Evolving Activity of Nickel Phosphide (0001) Surfaces. *ACS Catal.* **2017**, *7*, 7718−7725.
(56) Sheng, W.; Gasteiger, H. A.; Shao-Horn, Y. Hydrogen Oxidation and Evolution Reaction Kinetics on Platinum: Acid vs Alkaline Electrolytes. *J. Electrochem. Soc.* **2010**, *157*, B1529.
(57) Nørskov, J. K.; Bligaard, T.; Logadottir, A.; Kitchin, J. R.; Chen, J. G.; Pandelov, S.; Stimming, U. Trends in the Exchange Current for Hydrogen Evolution. *J. Electrochem. Soc.* **2005**, *152*, J23.
(58) Hellstern, T. R.; Benck, J. D.; Kibsgaard, J.; Hahn, C.; Jaramillo, T. F. Engineering Cobalt Phosphide (CoP) Thin Film Catalysts for Enhanced Hydrogen Evolution Activity on Silicon Photocathodes. *Adv. Energy Mater.* **2016**, *6*, 1501758−1501766.
(59) Alkire, R. C.; Bartlett, P. N.; Lipkowski, J.; Tanzirul Alam, M. *Advances in electrochemical sciences and engineering*; Wiley: Hoboken, NJ, 2015; Vol. *16* (Electrochemistry of carbon electrodes).
(60) Ma, L.; Ting, L. R. L.; Molinari, V.; Giordano, C.; Yeo, B. S. Efficient hydrogen evolution reaction catalyzed by molybdenum carbide and molybdenum nitride nanocatalysts synthesized via the urea glass route. *J. Mater. Chem. A* **2015**, *3*, 8361−8368.

DOI: 10.1021/acscatal.7b04466
ACS Catal. 2018, 8, 4408−4419